

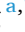


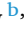





Metal passivation strengthens the interface in titanium composites reinforced with boron nitride nanotubes

Zihan Liu^{a,1} , Ning Li^{b,1} , Yingchun Jiang^{a,1} , Chenglin Yi^{a,1} , Cheol Park^c, Catharine C. Fay^c , Huck Beng Chew^{b,*} , Changhong Ke^{a,d,*} 

^a Department of Mechanical Engineering, State University of New York at Binghamton, Binghamton, NY 13902, USA

^b Department of Aerospace Engineering, University of Illinois at Urbana-Champaign, Urbana, IL 61801, USA

^c Advanced Materials and Processing Branch, NASA Langley Research Center, Hampton, Virginia 23681, USA

^d Materials Science and Engineering Program, State University of New York at Binghamton, Binghamton, NY 13902, USA

ARTICLE INFO

Keywords:

Boron nitride nanotubes (BNNTs)
Metal matrix composite (MMC)
Metal passivation
nanomechanics
interfacial interactions

ABSTRACT

We investigate the interfacial interaction in titanium metal matrix composites (MMCs) reinforced with boron nitride nanotubes (BNNTs) through in situ scanning electron microscopy nanomechanical pullout experiments. The measurements reveal a stronger interface formed by Ti with BNNTs than carbon nanotubes (CNTs). Density functional theory (DFT) calculations reveal that the observed interfacial strength is attributed to covalent bonding formed on the metal surface that is partially oxidized due to passivation. Moreover, the composite interface maintains its strength even after prolonged thermal annealing in air, which is in stark contrast to the substantial degradation that occurs on the composite interface with CNTs. The complex interplay of metal passivation on the interfacial interaction and reinforcement opens a new avenue of exploiting metal passivation as an innovative active self-strengthening mechanism for nanotube-reinforced MMCs.

1. Introduction

The incorporation of nanofibers into metals holds great potential for enhancing their mechanical properties, which is critical for a variety of engineering applications, such as in the automotive, biomedical, and aerospace industries [1,2]. The key to strengthening nanofiber-reinforced metal matrix composites (MMCs) lies in the efficient load transfer at the fiber-matrix interface, which allows the nanofibers—like carbon nanotubes (CNTs) and hexagonal boron nitride nanotubes (BNNTs)—to impart their superior mechanical properties, far exceeding those of the metal matrix. BNNTs, in particular, are highly attractive as MMC fillers due to their remarkable structural and mechanical properties, as well as their superior thermal stability compared to CNTs. BNNTs can withstand temperatures up to 900 °C in air [3] and over 1800 °C in inert environments [4], whereas CNTs begin to oxidize at around 400 °C. Moreover, the covalent and partially ionic characteristics of the B-N bonding result in a highly polarized electronic structure, giving BNNTs a stronger binding affinity [5,6] than CNTs that comprise neutral, covalent C-C bonds. This higher binding affinity

enhances load transfer at the BNNT-metal interface. Complex physio-chemisorption phenomena, including oxide formation on the metal surface due to passivation and thermal treatment, play a significant role in the interfacial bonding between nanofillers and metal matrices [7–11]. This passivation effect is especially important for active metals like titanium (Ti), which is known for its lightweight and high strength, making it an important aerospace material. However, the intricate relationship between metal passivation and nanofiller reinforcement in MMCs remains elusive.

In this work, we present the first direct and quantitative nanomechanical assessment of the BNNT-Ti interface using in situ scanning electron microscopy (SEM) experiments of pulling out individual nanotubes combined with density functional theory (DFT) calculations. The measurements reveal that the interfacial shear stress (IFSS) of the BNNT-Ti interface is approximately 56.2 MPa, representing an increase of about 49% in strength compared to the CNT-Ti interface. Notably, the composite interface retains its strength after thermal annealing at 800 °C in air. DFT calculations reveal the roles of both interfacial physio- and chemisorption interactions, as well as the strengthening effect of the

* Correspondence author.

E-mail addresses: hbchew@illinois.edu (H.B. Chew), cke@binghamton.edu (C. Ke).

¹ Authors contributed equally to this work.

oxide layer. These findings suggest that BNNT-metal interfaces exhibit enhanced load transfer capabilities, revealing a new self-strengthening mechanism in BNNT-MMC facilitated by metal passivation.

2. Results and discussion

2.1. Single-nanotube pullout measurements

Fig. 1a provides a schematic representation of the single-nanotube pullout measurement. A single protruding BNNT, partially embedded between two electron-beam-deposited metal layers, is pulled out using an atomic force microscopy (AFM) cantilever force sensor attached to a 3D nanomanipulator (details in Materials and Experimental Methods in the Supplement and Supplementary Fig. S1-S5). The BNNTs, synthesized using high-temperature pressure methods [12], exhibit high crystallinity and are predominantly double-walled structures with median diameter of 2.9 nm [13]. The SEM snapshots in Fig. 1b show one typical pullout measurement, where a single nanotube is fully extracted from the metal film. Additionally, scenarios of partial nanotube fracture are observed, mostly in the telescopic pullout scenarios (Fig. 1c), where the outermost shell of the nanotube is fractured, allowing the inner pristine shell(s) to slide out. As the binding interface between the matrix and the fractured outer nanotube shell remains intact inside the matrix, these fracture events and telescopic pullout measurements do not provide direct insight into the nanotube-matrix interfacial strength properties.

Fig. 2 presents the pullout force measurements from 29 successful single-nanotube pullout tests. Initially, the force increases with the embedded length of the BNNT, then plateaus at $\sim 407 \pm 77$ nN, indicating that load transfer at the BNNT-Ti interface follows a shear-lag behavior [14]. For comparison, prior data on CNT-Ti interfaces, obtained using the same methods (black triangles in Fig. 2, also see Materials and Experimental Methods in the Supplement) [9], shows a similar bilinear trend, but with a much lower plateau force of ~ 245 nN. Accounting for the differences in nanotube diameters (2.9 nm for BNNTs vs. 3.1 nm for CNTs), the load-bearing capacity of the BNNT-Ti interface, which is calculated as the ratio of the pullout load at the junction of the bilinear fitting curve in Fig. 2 and the entire interface area, is approximately 65%

higher on a per-unit-area basis. The initial rising portion of the force curve suggests an interfacial shear stress (IFSS) of ~ 56.2 MPa for the BNNT-Ti interface, which is about 49% higher than that of the CNT-Ti interface (~ 37.8 MPa) [9], highlighting the stronger bonding between BNNT and Ti. We also conducted pullout measurements on the same BNNT-Ti samples after thermal annealing at 800°C for 2 h in air (details in Supplementary Materials), as shown in Fig. 2 (empty stars). The results indicate that the composite interface retains its strength after thermal processing, in stark contrast to the CNT-Ti composite, which exhibits a $\sim 40\%$ reduction in interfacial strength after annealing at 400°C [11]. These findings emphasize the superior reinforcement potential of BNNTs in metal composites under high-temperature conditions and underscore the differing effects of thermal oxidation on load transfer in fiber-reinforced MMCs, which critically influence their bulk mechanical properties.

2.2. Materials characterization of metal oxidation

We perform material characterization to gain insights into the phase and morphological changes at the BNNT-Ti composite interface. AFM measurements (Fig. S2) show that the deposited Ti film (~ 200 nm thick) increases in thickness to ~ 277 nm after thermal annealing, likely due to the formation of rutile-phase titanium dioxide (TiO_2), as confirmed by Raman spectroscopy (Fig. S5). This $\sim 38.5\%$ volume expansion in the annealed Ti film is lower than the $\sim 58.7\%$ typically reported for complete Ti-to- TiO_2 conversion [15], indicating that the Ti film undergoes partial oxidation, with approximately 66% of Ti converted to TiO_2 . The annealing process also increases the grain size, from ~ 26 nm to ~ 29 nm (Fig. S1). Oxidation is known to initiate at grain boundaries, where oxygen diffusion is facilitated by higher energy states and defect densities [16], while it progresses more slowly within the grain interiors due to tighter atomic packing and restricted oxygen diffusion through the external oxide layer [17]. Additionally, the oxide layer inhibits the formation of reaction products such as TiB or TiB_2 at the BNNT-Ti interface [18–20], as confirmed by Raman measurements (Fig. S5). The schematic in Fig. 1a illustrates the BNNT-Ti interface morphology, showing partial oxide formation before annealing due to metal

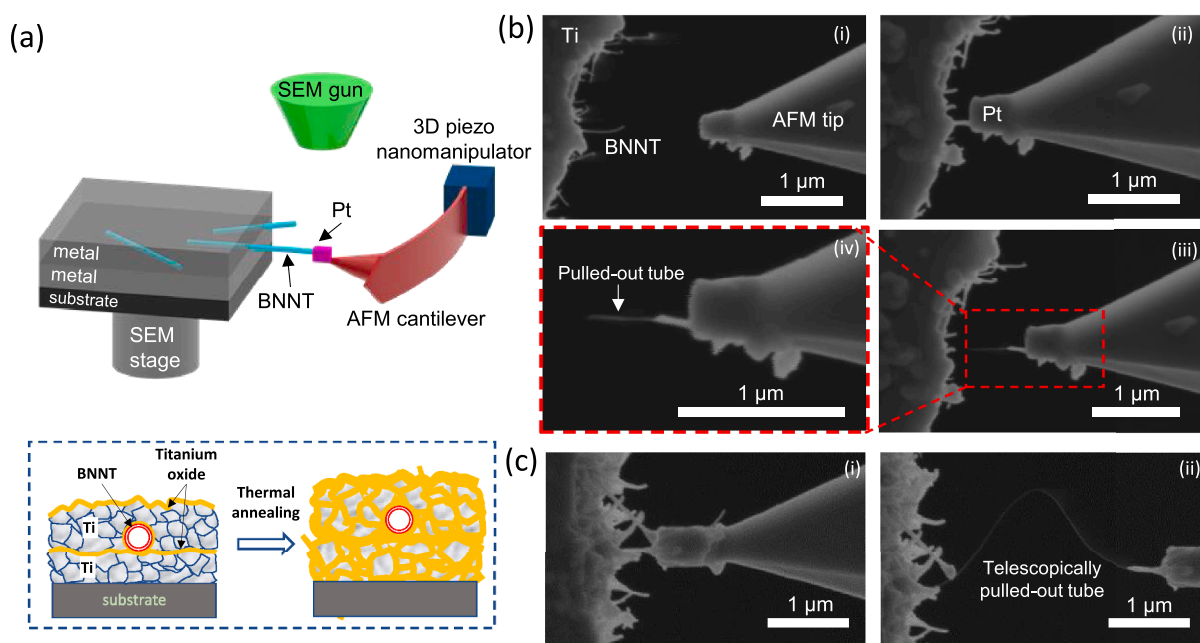


Fig. 1. *In situ* scanning electron microscopy nanomechanical single-nanotube pullout measurements of BNNT-Ti interfaces: (a) schematic of the testing setup; the bottom drawings illustrate the morphology transition of the BNNT-Ti interface after thermal annealing (all drawings are not to scale); (b) Selected SEM snapshots of a successful single nanotube pullout from Ti metal films (the pullout force ~ 146 nN and the embedded nanotube length ~ 392 nm); (c) Selected SEM snapshots of a telescopic pullout scenario.

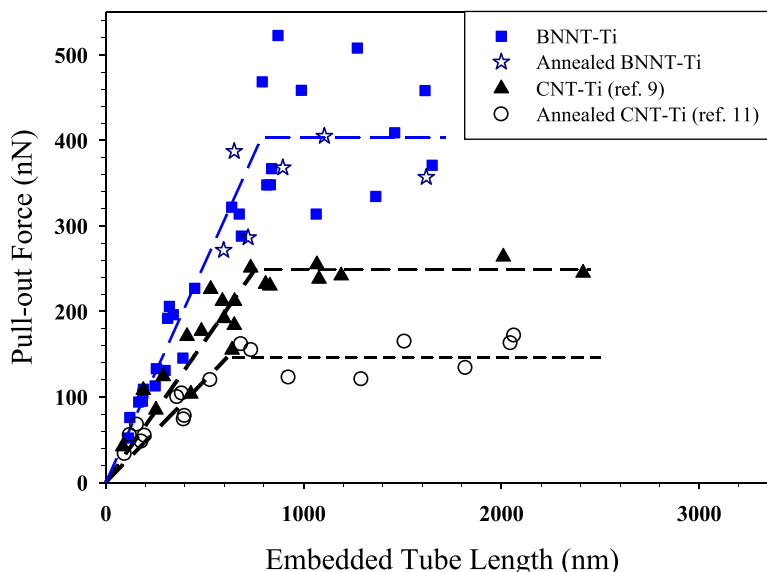


Fig. 2. The measured dependence of the pullout force on the embedded nanotube length for thermally annealed (blue empty stars) and non-annealed (blue solid squares) BNNT - Ti interfaces and the comparison with the reported data on CNT-Ti interfaces that are reproduced from *ref. 9* and *ref. 11*. The dashed lines are the respective bilinear fitting curves of the experimental data sets.

passivation, and significantly more oxide accumulation after annealing. The interface measurements of the annealed BNNT-Ti composite reveal the interfacial interaction between BNNT and TiO_2 .

2.3. Density functional theory calculations

To characterize the nanotube-matrix interfacial properties, we perform DFT calculations on monolayer graphene or hexagonal boron nitride (hBN) on crystalline Ti surfaces, and oxygen (O)-terminated bulk rutile TiO_2 surfaces. These model systems represent two limiting cases of various possible oxidation states of the Ti matrix [6,7,9,10] from its bare metal form to its fully oxidized state, where subsurface O diffusion results in the formation of thick bulk oxide interphases (TiO_2) (details in the Computational Method in the Supplement). *Fig. 3* shows the fully relaxed atomic configurations for all four model structures, accompanied by electron localization function (ELF) contours ranging from 0 to 1 along a vertical cross-section, which depict the probability of finding an electron near another electron with the same spin. At the Ti-graphene and Ti-hBN interfaces, moderate ELF values (depicted in green) are

observed, with average interfacial distances of 2.10 Å and 2.22 Å, respectively. This suggests weak chemisorption along these interfaces, which is consistent with previous findings [21]. Once oxidation transforms the pure Ti substrate to TiO_2 , we now observe contrasting differences in the interfacial interactions of hBN and graphene with the oxidized (TiO_2) interface. The interfaces for TiO_2 -graphene are cleanly delineated with an average separation distance of 2.60 Å, suggesting that oxidation considerably weakens the binding interactions, which are now predominantly van der Waals forces. In the case of the TiO_2 -hBN interface, the polarizing effect of the highly electronegative oxygen atoms interacting with the already polarized boron atoms in the hBN structure causes localized electron pockets to appear near the O-terminated surface. This results in the formation of strong chemical (covalent) B-O bonds across the TiO_2 -hBN interface, which reduces the mean interfacial separation distance by 11.3% to approximately 1.97 Å. These B-O covalent bonds alternate with weak N-O physisorption interactions to induce atomistic undulations in the hBN sheet (*Fig. 3d*). In our TiO_2 -hBN supercell (close-up view in *Fig. 3d*), seven B-O bonds are formed, each with bond lengths between 1.49 Å and 1.51 Å, which is

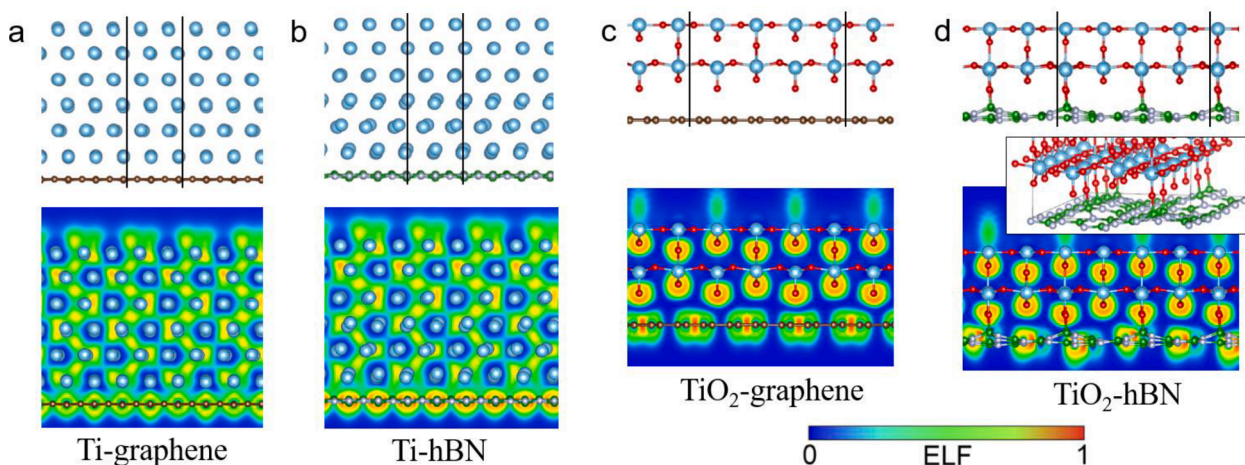


Fig. 3. Relaxed atomistic configurations of Ti-graphene (a), Ti-hBN (b), TiO_2 -graphene (c), and TiO_2 -hBN (d) model interfaces, with contours of the corresponding electron localization function (ELF) along a vertical cross-sectional cut. Inset in (d): close-up view of the B-O covalent bonding across TiO_2 -graphene. Atom colors: blue (Ti), brown (C), green (B), white (N), red (O). Solid back lines: periodic domain of DFT supercell.

comparable to previously reported tetrahedral B-O bond length of 1.45–1.47 Å [22,23]. The formation of these B-O bonds slightly stretches the adjacent B-N bonds in hBN, increasing their lengths to as much as 1.54 Å, compared to the equilibrium B-N bond length of 1.45 Å in free-standing hBN [24]. The N-B-O and N-B-N bond angles deviate by less than 6° from the 109.5° bond angles characteristic of tetrahedral structures. These results suggest the formation of sp^3 bonds across the TiO_2 -hBN interface.

The dramatic changes in the interfacial bonding characteristics due to oxidation are further reflected in the adhesion energies calculated by DFT. We determine the adhesion energy along the interfaces of each supercell by rigidly separating the relaxed configuration of each substrate and atomic sheet by 8 Å, and computing the per-unit-area difference in total energy between the isolated substrate and sheet from the combined structure. For Ti-graphene and Ti-hBN, we obtain comparable adhesion energies of 16.5 eV/nm² and 10.8 eV/nm², respectively. However, with an oxidized interface, the binding energy for TiO_2 -graphene decreases five-folds to 3.34 eV/nm², but dramatically increases two-folds to 20.5 eV/nm² for TiO_2 -hBN. It is noteworthy that our calculated binding energy for Ti-graphene is 4.6% higher than the reported value of 15.8 eV/nm², while the binding energy for TiO_2 -graphene is 7.7% lower than the reported value of 3.62 eV/nm², obtained using the Ceperley-Alder form of the local density approximation (LDA) [10].

Because of metal passivation, the interfaces of the Ti matrix are partially oxidized, with load transfer properties that span between those of pure Ti and O-terminated TiO_2 . The stronger binding of the hBN

atomic sheet with TiO_2 compared to pure Ti reflects the role of surface oxidation in enhancing the binding strength across the sheet-substrate interface. Since B-N bonds are already highly polarized within hBN, the electronegativity differences are now exacerbated between the terminating O atoms of the TiO_2 substrate and the B atoms within hBN, which promote the formation of strong B-O covalent bonds across the interface. However, graphene exhibits a different trend: metal passivation reduces its interaction with the substrate. This is because graphene consists of purely nonpolar C-C bonds, making it less reactive with the O atoms that are already interacting with Ti to form a stable structure [10,25–27]. These behaviors explain the contrasting results of our annealed nanotube pullout experiments (Fig. 2).

The mechanisms governing the pullout of CNTs and BNNTs from the partially oxidized Ti matrix are closely linked to the bonding properties across the interface. For graphene or hBN on pure Ti, interfacial sliding tends to be the primary failure mode. We generate the potential energy landscapes for interlayer sliding of graphene and hBN on the pure Ti matrix in Fig. 4a, by incrementally displacing the atomic sheets of graphene and hBN relative to pure Ti matrix substrate at 20 evenly spaced intervals along the two in-plane lattice vectors of each supercell, while allowing atomic relaxation in the vertical direction at each step. In both scenarios, the binding energy is approximately an order of magnitude greater than the maximum sliding barrier energy, suggesting that shear-induced interfacial sliding is the prevailing failure mode. When the pullout force is low, interfacial sliding occurs along minimum energy pathways, indicated by the dashed black lines in Fig. 4a. Conversely, a larger pullout force typically leads to rapid interfacial sliding along a

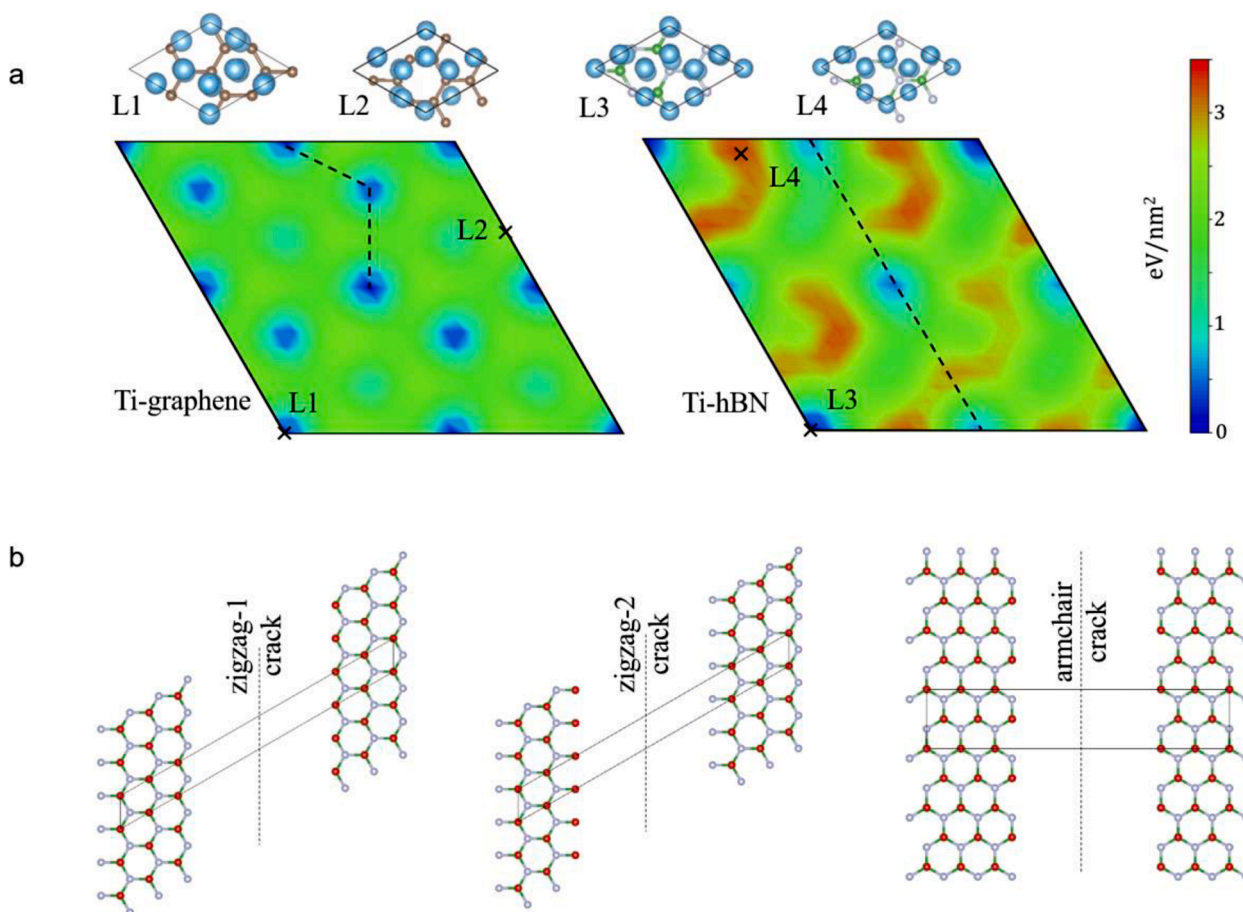


Fig. 4. (a) Contours of the interface sliding energy landscapes for Ti-graphene and Ti-hBN, with dashed lines denoting sampling of minimum energy pathways; energy contours plotted relative to the binding energy for Ti-hBN. (L1,L3) and (L2,L4) denote minimum energy and maximum sliding barrier energy locations, with corresponding atomistic configurations as viewed from the top. (b) Rigid separation of atoms for work of separation calculations to simulate crack formation along the armchair and two possible zigzag directions for O-doped hBN; solid lines denote periodic DFT supercell.

direct path, surpassing the peak energy barriers (L2, L4). Notably, both the minimum and peak energy barriers are slightly lower for the Ti-graphene interface compared to Ti-hBN, resulting in higher pullout forces for the latter.

In the case of TiO₂-graphene, the weak van der Waals interfacial interactions result in negligible energy barriers for both interfacial sliding and deadhesion, and negligible interfacial load transfer is expected. In contrast, binding between TiO₂-hBN is exceedingly strong, but the deformation will be highly localized near the B-O covalent bonds across the interface. Ultimately, there are two possible failure scenarios: the B-O bonds can break, or the B-N tube can locally fracture. The former is governed by the adhesion energy of 20.5 eV/nm² for TiO₂-hBN which represents the work of separation for interfacial fracture. We elucidate the possibility of sheet fracture by quantifying the work of separation along the two possible zigzag directions (zigzag-1, -2) and the armchair direction of (a) pure hBN, and (b) hBN doped with O atoms at the B sites to approximate the B-O bonding in TiO₂-hBN (Fig. 4b). To this end, we model unit cells of hBN and O-doped hBN, and relax each of these supercells in DFT. We rigidly separate atoms along the crack face in the zigzag-(1,2) or armchair directions, and compute the work of separation from the difference in total energy per unit crack area (crack length × assumed hBN sheet thickness of 3.33 Å). Along the (zigzag-1, -2, armchair) directions, we obtain a work of separation of (81, 114, 66) eV/nm² for pure hBN and (31, 67, 40) eV/nm² for O-doped hBN. This 40 to 60% difference in the work of separation is due to the presence of B-O bonds and the associated sp² to sp³ bond transitions with neighboring N atoms in hBN. Since cracks will form along the weakest path (zigzag-1 for TiO₂-hBN), the estimated fracture resistance for B-N bond breaking within hBN is ~31 eV/nm², which is comparable to the ~21 eV/nm² adhesion energy for B-O bond breaking along the TiO₂-hBN interface. Thus, both mechanisms of nanotube fracture and interface failure can be activated during the pullout of BNNT from an oxidized TiO₂ composite. This duality in possible failure mechanisms explains the notable fluctuations in the pull-out force measurements for both non-annealed and annealed BNNT-Ti in Fig. 2.

3. Conclusion

In summary, we explore the interfacial interaction in BNNT-reinforced Ti MMC using a combined experimental-computational approach. Our results reveal that BNNT exhibits a significantly stronger binding affinity with titanium compared to CNTs. This enhanced binding is primarily due to oxide formation on the metal surface from passivation, leading to robust covalent bonding along the BNNT-metal interface. Notably, this interface maintains its strength even after prolonged thermal annealing at elevated temperatures. The findings suggest that metal passivation can be synergistically exploited as a new self-strengthening strategy via activating and enabling the superior interface bonding interactions and maximizing BNNT's reinforcing potentials as active fillers. This innovative approach is particularly relevant to metals of porous structures, such as those produced by additively manufactured (AM) techniques. By strategically introducing oxide at the filler-metal interface via porosity pathways, the engineering practicality and reliability of AM metals can be significantly improved. This research paves the way for advancements in the design and industrial applications of high-performance metal composites.

CRediT authorship contribution statement

Zihan Liu: Writing – review & editing, Writing – original draft, Investigation, Formal analysis. **Ning Li:** Writing – review & editing, Writing – original draft, Investigation, Formal analysis. **Yingchun Jiang:** Writing – review & editing, Writing – original draft, Investigation, Formal analysis. **Chenglin Yi:** Investigation, Formal analysis. **Cheol Park:** Writing – review & editing. **Catharine C. Fay:** Writing – review & editing. **Huck Beng Chew:** Writing – review & editing, Writing

– original draft, Supervision, Investigation, Formal analysis, Conceptualization. **Changhong Ke:** Writing – review & editing, Writing – original draft, Supervision, Investigation, Formal analysis, Conceptualization.

Declaration of competing interest

The authors declare that they have no known competing financial interests or personal relationships that could have appeared to influence the work reported in this paper.

Acknowledgments

The authors acknowledge the support of the National Science Foundation under Grant Nos. CMMI-2009134, 2406763, and 2425706 (CK) and CMMI-2009684, 2406764, and 2425707 (HBC). CK acknowledges the support of the SUNY System Administration under SUNY Research Seed Grant Award #241008. The use of the Advanced Cyberinfrastructure Coordination Ecosystem: Services & Support (ACCESS), through allocations MAT220005, MAT230069, MAT240041, MAT240043, along with Frontera resources at the Texas Advanced Computing Center (TACC) through allocation MSS22006, are gratefully acknowledged.

Supplementary materials

Supplementary material associated with this article can be found, in the online version, at doi:10.1016/j.mtla.2025.102366.

References

- [1] S.R. Bakshi, D. Lahiri, A. Agarwal, Carbon nanotube reinforced metal matrix composites - a review *Int. Mater. Rev.* 55 (2013) 41.
- [2] W. Wang, Y. Zhu, S. Liao, J. Li, Carbon nanotubes reinforced composites for biomedical applications, *BioMed Res. Int.* 2014 (2014) 518609.
- [3] X. Chen, C.M. Dmuchowski, C. Park, C.C. Fay, C. Ke, Quantitative characterization of structural and mechanical properties of boron nitride nanotubes in high temperature environments, *Sci. Rep.* 7 (2017) 11388.
- [4] M.J. Tank, A.N. Reyes, J.G. Park, L.R. Scammell, M.W. Smith, Leon A De, R. D. Sweat, Extreme thermal stability and dissociation mechanisms of purified boron nitride nanotubes: implications for high-temperature nanocomposites, *ACS Appl. Nano Mater.* 5 (2022) 12444–12453.
- [5] X. Chen, L. Zhang, C. Park, C.C. Fay, X. Wang, Ke C, Mechanical strength of boron nitride nanotube-polymer interfaces, *Appl. Phys. Lett.* 107 (2015) 253105.
- [6] N. Li, C.M. Dmuchowski, Y. Jiang, C. Yi, F. Gou, J. Deng, C. Ke, H.B. Chew, Sliding energy landscape governs interfacial failure of nanotube-reinforced ceramic nanocomposites, *Scr. Mater.* 210 (2022) 114413.
- [7] Y. Jiang, N. Li, Z. Liu, C. Yi, H. Zhou, C. Park, C.C. Fay, J. Deng, H.B. Chew, C. Ke, Exceptionally strong boron nitride nanotube aluminum composite interfaces, *Extreme Mech. Lett.* 59 (2023) 101952.
- [8] C. Yi, X. Chen, F. Gou, C.M. Dmuchowski, A. Sharma, C. Park, C. Ke, Direct measurements of the mechanical strength of carbon nanotube - Aluminum interfaces, *Carbon N Y* 125 (2017) 93–102.
- [9] C. Yi, S. Bagchi, C.M. Dmuchowski, F. Gou, X. Chen, C. Park, H.B. Chew, C. Ke, Direct nanomechanical characterization of carbon nanotubes - titanium interfaces, *Carbon N Y* 132 (2018) 548–555.
- [10] S. Bagchi, C. Ke, H.B. Chew, Oxidation effect on the shear strength of graphene on aluminum and titanium surfaces, *Phys. Rev. B* 98 (2018) 174106.
- [11] C.M. Dmuchowski, C. Yi, F. Gou, A. Sharma, C. Park, C. Ke, Oxidation weakens interfaces in carbon nanotube reinforced titanium nanocomposites: an in situ electron microscopy nanomechanical study, *Extreme Mech. Lett.* 41 (2020) 101045.
- [12] M.W. Smith, K.C. Jordan, C. Park, J.-W. Kim, P.T. Lillehei, R. Crooks, J.S. Harrison, Very long single- and few-walled boron nitride nanotubes via the pressurized vapor/condenser method, *Nanotechnology* 20 (2009) 505604.
- [13] V. Yamakov, C. Park, J.H. Kang, X. Chen, C. Ke, C. Fay, Piezoelectric and elastic properties of multiwall boron-nitride nanotubes and their fibers: a molecular dynamics study, *Comput. Mater. Sci.* 135 (2017) 29–42.
- [14] K.R. Jiang, L.S. Penn, Improved analysis and experimental evaluation of the single filament pull-out test *Compos. Sci. Technol.* 45 (1992) 89–103.
- [15] W. Li, X. Jin, F. Huang, G.Z. Chen, Metal-to-oxide molar volume ratio: the overlooked barrier to solid-state electroreduction and a "Green" bypass through recyclable NH₄HCO₃, *Angew. Chem. Int. Ed.* 49 (2010) 3203–6.
- [16] M. Shi, Y. Takayama, H. Kato, Effect of surface microstructure of titanium sheet on the photocatalytic activity of its oxide film, *Mater. Trans.* 48 (2007) 1523–8.
- [17] A. Undisz, F. Schrempel, W. Wesch, M. Rettenmayr, Mechanism of oxide layer growth during annealing of NiTi *J. Biomed. Mater. Res. A* 100A (2012) 1743–1750.

- [18] M.M.H. Bhuiyan, J. Wang, L.H. Li, P. Hodgson, A. Agarwal, M. Qian, Y. Chen, Boron nitride nanotube reinforced titanium metal matrix composites with excellent high-temperature performance, *J. Mater. Res.* 32 (2017) 3744–3752.
- [19] K. Aniolek, The influence of thermal oxidation parameters on the growth of oxide layers on titanium, *Vacuum* 144 (2017) 94–100.
- [20] J. Bustillos, X. Lu, P. Nautiyal, C. Zhang, B. Boesl, A. Agarwal, Boron nitride nanotube–reinforced titanium composite with controlled interfacial reactions by spark plasma sintering, *Adv. Eng. Mater* 22 (2020).
- [21] C. Rohmann, Q. Sun, D.J. Searles, Interaction of Al, Ti, and Cu atoms with boron nitride nanotubes: a computational investigation, *J. Phys. Chem. C* 120 (2016) 3509–3518.
- [22] W.H. Zachariasen, The crystal structure of monoclinic metaboric acid, *Acta Crystallogr* 16 (1963) 385–9.
- [23] Z. Bai, L. Liu, D. Wang, C.-L. Hu, Z. Lin, To improve the key properties of nonlinear optical crystals assembled with tetrahedral functional building units, *Chem. Sci.* 12 (2021) 4014–4020.
- [24] S. Majety, X.K. Cao, R. Dahal, B.N. Pantha, J. Li, J.Y. Lin, H.X. Jiang, Semiconducting hexagonal boron nitride for deep ultraviolet photonics, *Proc. SPIE* 8268 (2012) 82682R.
- [25] F. Hennrich, R. Krupke, K. Arnold, J.A. Rojas Stütz, S. Lebedkin, T. Koch, T. Schimmel, M.M. Kappes, The mechanism of cavitation-induced scission of single-walled carbon nanotubes, *J. Phys. Chem. B* 111 (2007) 1932–7.
- [26] S. Ayissi, P.A. Charpentier, N. Farhangi, J.A. Wood, K. Palotás, W.A. Hofer, Interaction of titanium oxide nanostructures with graphene and functionalized graphene nanoribbons: a DFT study, *J. Phys. Chem. C* 117 (2013) 25424–25432.
- [27] P.M. Martins, C.G. Ferreira, A.R. Silva, B. Magalhães, M.M. Alves, L. Pereira, P. A. P. Marques, M. Melle-Franco, S. Lanceros-Méndez, TiO₂/graphene and TiO₂/graphene oxide nanocomposites for photocatalytic applications: a computer modeling and experimental study *Compos, Part B Eng* 145 (2018) 39–46.